Thermal Transport in Phase-Stabilized Lithium Zirconate Phosphates

Sajad Yazdani,[1] Raana Kashfi-Sadabad,[2] Mayra Daniela Morales-Acosta,[3] Raul David Montaño,[4] Tuoc Ngoc Vu,[5] Huan Doan Tran,[6] Menghan Zhou,[7] Yufei Liu,[7] Jian He,[7] and Michael Thompson Pettes[8,a)]

[1] Department of Mechanical Engineering and Materials Science and Energy Sciences Institute, Yale University, New Haven, Connecticut 06511, USA
[2] School of Medicine, Stanford University, Stanford, California 94305, USA
[3] Institute of Materials Science, University of Connecticut, Storrs, Connecticut 06269, USA
[4] Department of Mechanical Engineering, The University of Texas at Austin, Austin, Texas 78712, USA
[5] Department of Theoretical Physics and Institute of Engineering Physics, Hanoi University of Science and Technology, Hanoi 10000, Vietnam
[6] School of Materials Science and Engineering, Georgia Institute of Technology, Atlanta, Georgia 30332, USA.
[7] Department of Physics and Astronomy, Clemson University, Clemson, South Carolina 29634, USA
[8] Center for Integrated Nanotechnologies (CINT), Materials Physics and Applications Division, Los Alamos National Laboratory, Los Alamos, New Mexico 87545, USA
[a)] Author to whom correspondence should be addressed: pettesmt@lanl.gov

Abstract. The thermal properties of yttrium-stabilized lithium zirconate phosphate (LZP: $Li_{1+x+y}Y_xZr_{2-x}(PO_4)_3$ with $x = 0.15$, $-0.2 \leq y \leq 0.4$ and with $x = 0.0$, $y = 0.0$) are presented over a wide temperature range from 30 to 973 K, elucidating the interplay between structural phase transformations and thermal properties in a solid state superionic conducting material. At room temperature, the thermal conductivity decreases by more than 75 % as the stoichiometry is changed from lithium deficient to excess, and increases with increasing temperature indicative of defect-mediated transport in the spark plasma sintered materials. The phase transformations and their stabilities are examined by x-ray diffraction and differential scanning calorimetry and indicate that the Y^{3+} substitution of Zr^{4+} is effective in stabilizing the ionically conductive rhombohedral phase over the entire temperature range measured, the mechanism of which is found through *ab initio* theoretical calculations. These insights into thermal transport of LZP superionic conductors are

valuable as they may be generally applicable for predicting material stability and thermal management in the ceramic electrolyte of future all-solid-state-battery devices.

Main Text

Using elemental lithium (Li) as anodes will be highly advantageous in electrochemical energy storage devices in terms of the capacity and cell voltage[1], however the main challenge preventing this beneficial anode from use in batteries is the formation of un-wanted Li-dendrites during the charge and discharge cycles[2]. The solution to this challenge is to design electrolytes that are mechanically robust enough to block dendrite propagation while simultaneously allowing fast conduction of ions[3-9]. Using solid ion conducting electrolytes will enable this fast charge-discharge[1], however, cycling at high rates will be hindered if the large amount of inevitable heat generated by Joule heating is not accounted for in cell design[10, 11]. Relevant to applications, improved thermal stability and thermal conductivity of solid state electrolytes will mitigate the most severe limitations of these materials by allowing operation at higher temperatures and reducing hot spots[12]. However, thermal conductivity (κ) data for these materials is sparse and only available for few ionic conductors such as lithium iodate (α-$LiIO_3$) and lithium tetraborate ($Li_2B_4O_7$) which show room temperature $\kappa \sim 3.5$–4 W m^{-1} K^{-1} that increases with increasing temperature to ~ 450 K[13, 14]; lithium aluminum germanium phosphate glass–ceramics [$Li_{1+x}Al_xGe_{2-x}(PO_4)_3$] which show room temperature $\kappa \sim 0.8$–1.8 W m^{-1} K^{-1} that is nearly temperature independent to ~ 973 K[15]; Li_2SO_4 and Ag_2SO_4 which show room temperature $\kappa \sim 0.3$–0.5 W m^{-1} K^{-1} that increases slightly with increasing temperature to ~ 650 K[16]; and $LiCuVO_4$ which shows room temperature $\kappa \sim 5$ W m^{-1} K^{-1} that increases with increasing temperature[17] similar to other quasi-1D superionics $LiIO_3$ and $Li_2B_4O_7$.

Among various oxides, lithium superionic conductor (LISICON)-type electrolytes such as lithium zirconate phosphate (LZP) are suitable for high-voltage solid-state batteries[1, 9]. A general formulation for the LZP crystal structure is $Li_{1+x}Zr_{2-x}M_x(PO_4)_3$, where M = Al, Ca, Cr, Ga, Fe, Sc, In, Lu, Y or La[1, 18-25]. Early transition metals such as Zr^{4+} have no electron in their *d*-orbital and therefore will not contribute to the electrical conductivity[22]. In a LISICON-type structure, MO_6 octahedra are interconnected with PO_4 tetrahedra by corner sharing, forming the skeleton of the structure. Lithium conduction occurs by hopping between two sites; one located directly between two MO_6 octahedra and the other one positioned between two columns of MO_6 octahedra. Among LISICON-type materials, $LiZr_2(PO_4)_3$ ceramics have been shown to form rhombohedral ($R\bar{3}c$) structures with promising ionic conductivity on the order of 10^{-4} Scm^{-1} [26], although the triclinic ($P\bar{1}$) phase of this material possesses low ionic conductivity on the order of 10^{-8} S cm^{-1} [27]. The dominant materials challenge for these superionic conductors is that the triclinic phase is thermodynamically favored at normal battery operating temperatures. The ion-conducting rhombohedral phase is not stable over battery operating temperature ranges as a triclinic-to-rhombohedral phase transition takes place at temperatures above 310 K[28] (reported in the range from 300 to 340 K[29, 30]). Recent advances have identified empirical evidence for defect-stabilized rhombohedral LZP-based materials using, for example, a Zr-acetate[3] precursor or substitution of Zr^{4+} with Y^{3+} [26] or Ca^{2+} [23-25]. Li and Goodenough *et al.*[3] reported the development of a LZP solid electrolyte with a high effective ionic conductivity of $\sigma_{Li} = 2 \times 10^{-4}$ S cm^{-1} at 25 °C, and a high electrochemical stability up to 5.5 V versus Li^+/Li [3]. A thin amorphous interfacial layer of Li_8ZrO_6 and Li_3P was formed on the $LiZr_2(PO_4)_3$ surface due to reaction with Li metal. This interfacial layer was wet by Li metal and suppressed the Li dendrite propagation. These promising results motivate the present work to investigate the thermal properties of transition-metal stabilized LZP.

Here, we report the phase stability and thermal conductivity of $Li_{1+x+y}Y_xZr_{2-x}(PO_4)_3$ (x = 0.15, $-0.2 \leq y \leq 0.4$ and $x = 0.0$, $y = 0.0$) ceramics over a wide temperature range from 30 to 973 K. Stabilization of the rhombohedral phase is confirmed by substitution of Zr^{4+} by Y^{3+} (denoted as x) and where the charge imbalance caused by this substitution is taken into account by adding x equivalent charges from excess Li^+. Moreover, various lithium concentration quantities are used in order to investigate the effects of Li excess or deficiency (denoted as y) on the phase stability.

The room temperature x-ray diffraction (XRD) patterns for the $Li_{1+x+y}Y_xZr_{2-x}(PO_4)_3$ samples are shown in Fig. 1. The crystallographic structures reported for rhombohedral structure of $LiZr_2(PO_4)_3$ [$R\bar{3}c$ (167)],[31] triclinic $LiZr_2(PO_4)_3$ [$P\bar{1}$ (2)],[32], monoclinic $LiZr_2(PO_4)_3$ [$P2_1/c$ (14)],[33] tetragonal YPO_4 [$I4_1/amd$ (141)],[34] and cubic ZrP_2O_7 [$Pa\bar{3}$ (205)][35] were adopted as a starting structural model in the Rietveld analysis. The peak profile and background were fitted using a pseudo-Voigt and a nine-term Chebyschev polynomial, respectively. The instrument parameters were derived from a refinement using a NIST LaB_6 standard. Satisfactory structure refinements were obtained by varying the lattice parameters, phase fraction, microstrain, and crystallite size terms. Site occupancies, atomic positions and thermal factors, were fixed as the quality of the refinement was adequate for quantitative analysis. The graphics of the Rietveld analysis for the Li-deficient sample ($x = 0.15$, $y = -0.2$) and the sample with excess Li ($x = 0.15$, $y = 0.2$) are shown in Figs. S1 and S2 in the supplementary material, respectively. The crystalline phases present in each sample, refined lattice parameters, weight percentages and reliability factors are detailed in Table S1, supplementary material.

In order to investigate the effects of Y^{3+} substitution, we analyzed the Rietveld refined XRD data of the samples with and without Y. In the sample with no Y^{3+} ($x = 0.0$, $y = 0.0$), only 12.9 wt.% of the sample was found to be in the rhombohedral phase and the rest practically

consisted of the triclinic phase. In contrast, the sample with Y^{3+} substitution ($x = 0.15$, $y = 0.0$) was composed of 97.5 wt.% rhombohedral phase with no sign of the triclinic phase, providing evidence for the effectiveness of the Y^{3+} substitution of Zr^{4+} for stabilizing the ionically conductive rhombohedral phase. In addition, several samples with less and more Li than the stoichiometric value were synthesized and analyzed in order to understand the effects of having excess Li *vs.* its deficiency. In the Li-deficient sample ($x = 0.15$, $y = -0.2$), only 36.5 wt.% rhombohedral phase was detected. Triclinic was the major phase (55.5 wt.%) along with minor formation of cubic ZrP_2O_7 (2.5 wt.%). Thus, it can be concluded that a lack of Li can destabilize the rhombohedral phase and favor formation of the triclinic phase, a result which should be accounted for in application. On the other hand, in the case of using excess Li ($x = 0.15$, $y = 0.2$, 0.4), the samples mainly consisted of rhombohedral phase (55.9 and 69.1 wt.%, respectively) with considerable monoclinic phase concentration (43.6 and 30.3 wt.%, respectively). Therefore, in addition to the rhombohedral phase, the deficiency and excess of Li favored formation of triclinic and monoclinic phases, respectively.

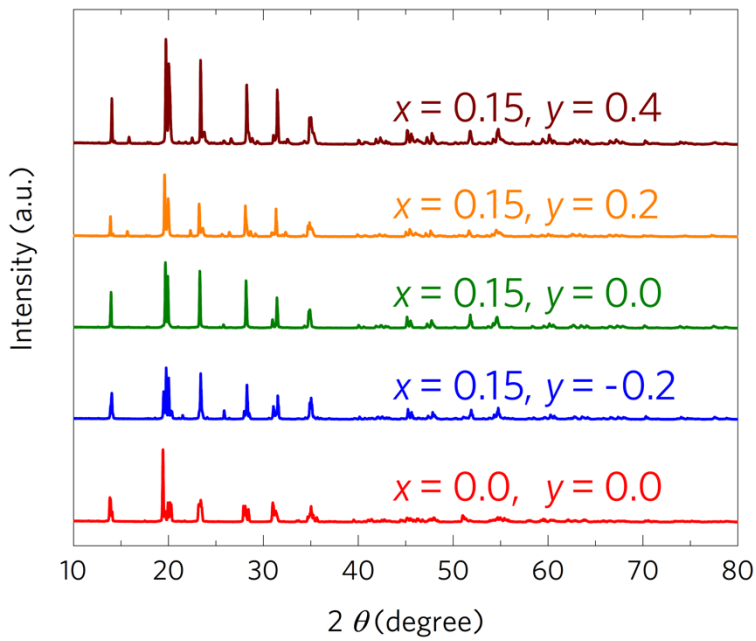

Fig. 1. X-ray diffraction patterns of the $Li_{1+x+y}Y_xZr_{2-x}(PO_4)_3$ samples in this work ranging from pure (x=0) to rhombohedral phase stabilized (x=0.15), and from lithium deficient to excess ($-0.2 \leq y \leq 0.4$).

Fig. 2(a) shows a representative pellet used for thermal diffusivity (α) measurements, and a representative rectangular bar used for low-temperature κ measurements which has been cut from the measured pellet. The low-temperature specific heat (c_p) and κ measurement data are shown in Fig. 2(b,c), respectively. Differential scanning calorimetry (DSC) measurements from 75.18 to 473.15 K indicated that samples with no triclinic phase ($x = 0.15$, $y = 0.0$, 0.4) experienced no phase transformation, and the rhombohedral phase was stable over this temperature range. In contrast, a major peak centered at 320.15 K was observed for the Li deficient sample with $x = 0.15$, $y = -0.2$ which was attributed to the triclinic phase transition. The $x = 0.15$, $y = 0.2$ sample exhibited a small peak at 338.15 K which can arise due to the larger monoclinic phase in this sample. The

low-temperature κ measurements from 20 to 300 K (taken perpendicular to the SPS press direction), showed an entirely different behavior for the Li-deficient sample ($x = 0.15$, $y = -0.2$) compared to the charge balanced sample ($x = 0.15$, $y = 0.0$) or the sample with excess Li ($x = 0.15$, $y = 0.2$). For the former, clear phonon-phonon scattering dominant behavior was detected whereas for the latter cases κ slightly increased with increasing temperature from 20 to 300 K. It is reasonable to attribute the different trends in κ to the dominance of the triclinic phase in Li-deficient samples and the dominance of the rhombohedral phase in the other samples.

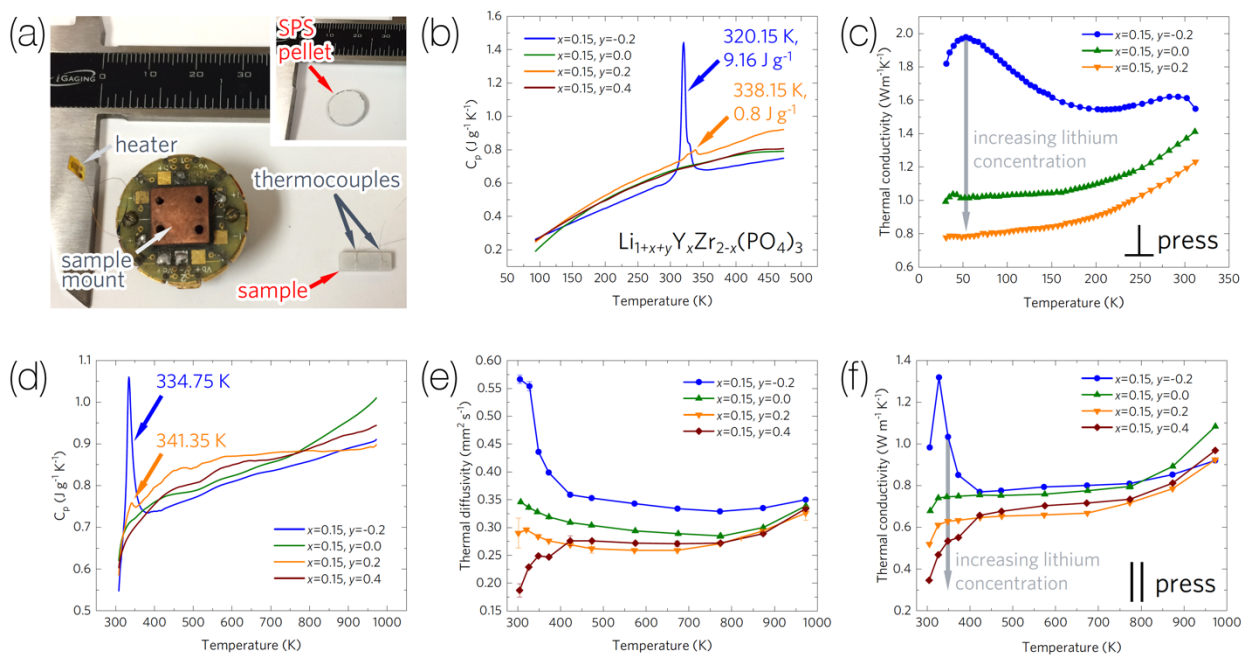

Fig. 2. Thermal properties of yttrium-stabilized lithium zirconate phosphate. (a) Overview of spark plasma sintered rectangular sample for low-temperature thermal conductivity measurements and (inset) circular pellet for laser flash measurements from which the rectangular bar was cut. Low-temperature (b) DSC measurements of specific heat, c_p, and (c) thermal conductivity data. High-temperature (d) DSC measurements, (e) thermal diffusivity data obtained from laser flash measurements, and (f) thermal conductivity of the samples.

High-temperature DSC measurements from 298 to 973 K are illustrated in Fig. 2(d). No phase transformation is observed for $x = 0.15$, $y = (0.0, 0.4)$ over the entire temperature range. Similar to the low-temperature measurements, a major peak at 334.75 K was detected for $x = 0.15$, $y = -0.2$, and minor peak at 341.35 K was detected for $x = 0.15$, $y = 0.2$. The slight difference in the peak locations detected over the common temperature range of low and high-temperature DSC data can be attributed to the different instruments used for each measurement[36].

Above-room-temperature α and κ data are shown in Fig. 2(e,f), respectively. For the Li-deficient sample ($x = 0.15$, $y = -0.2$), the α decreases from 0.57 $mm^2\ s^{-1}$ at room temperature to 0.35 $mm^2\ s^{-1}$ at 973 K. The α of the samples with $x = 0.15$, $y = (0.0, -0.2)$ slightly decreases then approaches a value of 0.34 $mm^2\ s^{-1}$ as the temperature increased to 973 K. The α of the sample with $x = 0.15$, $y = 0.4$ (sample with excess Li) increases over the entire temperature range to this value. The above-room-temperature κ of $x = 0.15$, $y = (0.0, 0.2, 0.4)$ samples steadily increased as the temperature was raised from 300 to 973 K, a trend reported for single-crystalline Li-based superionics[13, 14, 17] although in this work the magnitude of κ is lower and the temperature at which κ begins to increase is higher due to the polycrystalline nature of the materials. The room temperature κ values are on the order of those reported for sintered superionics[15].

For the stoichiometric sample with $x = 0.15$, $y = 0.0$, κ increases from 0.68 $W\ m^{-1}\ K^{-1}$ at room temperature to 1.1 $W\ m^{-1}\ K^{-1}$ at 973 K. The Li-deficient sample ($x = 0.15$, $y = -0.2$) exhibited a very different trend in κ in a small temperature range near room temperature, increasing rapidly to a maximum of 1.32 $W\ m^{-1}\ K^{-1}$ at 327.6 K [Fig. 2(f)] and then decreasing rapidly with increasing temperature. This rapid change in κ corresponded well to the triclinic-to-rhombohedral phase transformation that was observed to occur around 320–335 K by DSC [Fig. 2(b,d)]. After the

rhombohedral phase transformation occurred, κ rapidly approached that of the other samples. It should be noted that in order to obtain κ at both low and high-temperatures on each individual sample, high-temperature κ values are reported parallel to the SPS press direction, while low-temperature values are κ reported perpendicular to the SPS press direction owing to the experimental geometry required for each technique.

Fig. 3(a,b) illustrates a comparison between the temperature-dependent DSC measurements of three additional ($x = 0.15$, $y = 0.0$) samples to look at reproducibility of the experimental results. Samples 1 and 3 were measured by NETZSCH Instruments Testing Laboratory, Burlington, MA, on a NETZSCH model DSC 404 F1 *Pegasus*® differential scanning calorimeter and sample 2 was measured on a NETZSCH DSC 404 C in our laboratory. Despite being different samples from different synthesis batches, the obtained data were within ~7% of one another. Fig. 3(b,d) shows the thermal diffusivity measurements of $x = 0.15$, $y = 0.0$ samples 1 and 2, and two additional samples of $x = 0.15$, $y = 0.2$ representing two samples of each chemical composition from different synthesis batches. These measurements showed a maximum difference of 16.7% at 326 K and 6.2% at 573 K, respectively. Moreover, a maximum difference of 6.4% at 156 K was obtained for two thermal conductivity measurements of the $x = 0.15$, $y = 0.2$ samples over the entire temperature range from 30 to 312K [Fig. 3(d)]. The sample without Y substitution showed a phase change in the range from 300–345 K which caused an anomaly in κ (Fig. S3, supplementary material) but approached a value close to those obtained for the rest of the samples (0.72 W m^{-1} K^{-1} at 973 K).

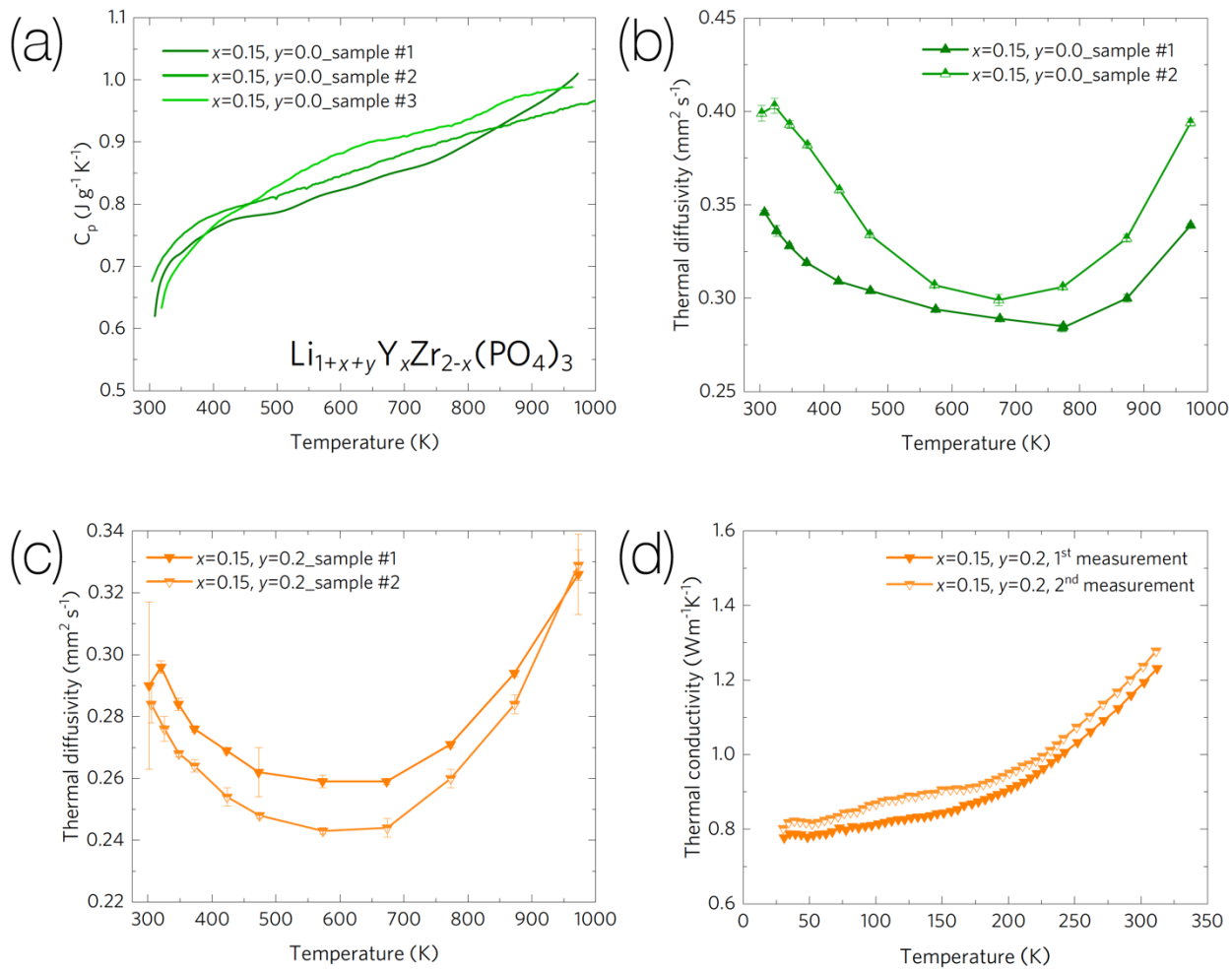

Fig. 3. Sample-to-sample and instrument-to-instrument variation in thermal measurements of rhombohedral $Li_{1+x+y}Y_xZr_{2-x}(PO_4)_3$. (a) DSC specific heat measurements of three different $x = 0.15$, $y = 0.0$ samples demonstrate reproducibility. Thermal diffusivity measurements of different samples from different synthesis batches of (b) $x = 0.15$, $y = 0.0$ and (c) $x = 0.15$, $y = 0.2$. (d) 1st run and 2nd run low-temperature thermal conductivity measurements of the $x = 0.15$, $y = 0.2$ sample.

The primary goal of our density functional theory (DFT)[37, 38] calculations is to understand the stabilization of the ion-conducting rhombohedral phase over the triclinic phase of yttrium-stabilized LZP when external perturbations that may come from experimental conditions, e.g., doping and pressure, are present. The DFT version implemented in the *Vienna Ab initio Simulation*

Package[39] was used for our calculations, employing the Perdew–Burke–Ernzerhof exchange-correlation functional[37, 38] and a plane-wave energy cutoff of 600 eV. A Monkhorst-Pack mesh of $7 \times 7 \times 7$ was used to sample the Brillouin zone, which, in our case, makes a fine k-point density of no larger than 0.025 π Å^{-1}. Using this numerical scheme, the experimentally resolved rhombohedral and triclinic structures were then relaxed until atomic forces were smaller than 0.01 eV Å^{-1}. The optimized lattice parameters of the examined structures were consistent with the measured values (Table S2, supplementary material). The DFT energy of the rhombohedral phase was about 13 meV atom^{-1} higher than the triclinic phase, confirming that the triclinic phase is indeed the ground state in the undoped sample. This energy difference however is small, being just about one half of the thermal energy per atom ($k_B T$ is ~26 meV at room temperature). Therefore, temperature could be one factor for the stabilization of the rhombohedral phase as evidenced by the experimental DSC results. However, the role of temperature was not considered in this work because of enormous computational resource needed; we instead focus on other major knowledge gaps relevant to materials engineering of yttrium-stabilized LZP superionic conductors.

Metastable phases of solids are often realized[40-43], but their stabilization is normally quite complicated and hard to be traced out. For example, the metastable *Pca2*$_1$ ferroelectric phase of HfO_2 – predicted by theory and recently experimentally realized – was found to be stabilized by not any single perturbation such as doping, but by an optimal combination of many factors including surface energy, strain, doping, and external electric field[44-46]. Pressure and stress were also found to stabilize numerous binary compounds of Mg and Si[4]. Therefore, we consider the effects of both Y-doping and external isotropic pressure on the thermodynamic favorability of the rhombohedral and triclinic phases of LZP. For such calculations, we used a 2×1×1 supercell of the primitive cell of these phases, both containing 4 formula units. One Zr atom was replaced by an Y

atom, leading to $x = 0.25$, being comparable with our experimental value of $x = 0.15$. For the rhombohedral phase, there is one inequivalent position of Zr while for the triclinic phase, there are two. In our calculations, all of these possible doping sites were considered.

The relative energy of these two phases is shown in Fig. S4, supplementary material, as a function of pressure. Y-doping dramatically elevates the relative energy of the triclinic phase from -13 to ~1 meV atom^{-1}, stabilizing the rhombohedral phase. Pressure, which may be realized locally during the synthesis of the material, such as near the surface and grain boundaries, also plays a significant role in stabilizing the undoped rhombohedral phase over the undoped triclinic phase, bringing the energy difference between them from 13 to about 4 meV atom^{-1}. We believe that the small energy differences uncovered by the theoretical calculations in this work are well within the recently introduced "amorphous limit"[47] that allows metastable solid phases (in this case the undoped rhombohedral phase) to become synthesizable.

In conclusion, the relationship between thermal transport and phase stability of yttrium-doped lithium zirconate phosphate solid state superionic conductors were reported in detail. X-ray diffraction showed that in the absence if Y^{3+}, the sample consisted of mainly the non-conductive triclinic LZP with only 12.9 wt.% of the ion-conducting rhombohedral phase. The specific heat, thermal diffusivity, and thermal conductivity were presented over a wide temperature range from 30–973 K, and varied from ~0.35 to 1.5 W m^{-1} K^{-1} at room temperature, which was found to depend strongly on the concentration of lithium. Apart from the importance of a detailed understanding of thermal properties of non-stoichiometric LZP solid-state electrolytes for thermal management in practical applications of all-solid-state-batteries, we hope that the current work inspires future investigations of thermal transport phenomena in superionic conductors including during fast charge and discharge operation.

See the supplementary material for additional details of experimental methods, complete x-ray diffraction and phase composition analysis, thermal analysis of pure LZP, and additional DFT results.

Acknowledgements

Experimental work and materials synthesis by M.T.P., S.Y., R.K.-S., and R.D.M. were supported by the U. S. National Science Foundation Award Nos. CAREER-1553987 (M.T.P., S.Y., and R.K.-S.) and REU-1560098 (M.T.P. and R.D.M.). This work was performed, in part, under user Grant No. 2018AU0060 at the Center for Integrated Nanotechnologies, an Office of Science User Facility operated for the U.S. Department of Energy (DOE) Office of Science and supported, in part, by the Laboratory Directed Research and Development program of Los Alamos National Laboratory under project number 20190516ECR (M.T.P.). Los Alamos National Laboratory, an affirmative action equal opportunity employer, is managed by Triad National Security, LLC for the U.S. Department of Energy's NNSA, under contract 89233218CNA000001. Theoretical and computational work by H.D.T. and T.N.V. was supported by XSEDE through the allocation number TG-DMR170031 (H.D.T.), and by Vingroup Innovation Foundation (VINIF) through project VINIF.2019.DA03 (T.N.V.).

Data Availability Statement

The data that supports the findings of this study are available within the article and its supplementary material. The crystallographic information files relaxed by DFT at zero pressure are also available at http://www.godeepdata.org/.

References

[1] A. Manthiram, X. Yu, and S. Wang, "Lithium battery chemistries enabled by solid-state electrolytes," Nat. Rev. Mater. **2**, 16103 (2017). https://doi.org/10.1038/natrevmats.2016.103

[2] W. Xu, J. Wang, F. Ding, X. Chen, E. Nasybulin, Y. Zhang, and J.-G. Zhang, "Lithium metal anodes for rechargeable batteries," Energy Environ. Sci. **7**, 513 (2014). https://doi.org/10.1039/C3EE40795K

[3] Y. Li, W. Zhou, X. Chen, X. Lü, Z. Cui, S. Xin, L. Xue, Q. Jia, and J. B. Goodenough, "Mastering the interface for advanced all-solid-state lithium rechargeable batteries," Proc. Natl. Acad. Sci. U. S. A. **113**, 13313 (2016). https://doi.org/10.1073/pnas.1615912113

[4] F. Zheng, M. Kotobuki, S. Song, M. O. Lai, and L. Lu, "Review on solid electrolytes for all-solid-state lithium-ion batteries," J. Power Sources **389**, 198 (2018). https://doi.org/10.1016/j.jpowsour.2018.04.022

[5] C. Monroe and J. Newman, "The Impact of elastic deformation on deposition kinetics at lithium/polymer interfaces," J. Electrochem. Soc. **152**, A396 (2005). https://doi.org/10.1149/1.1850854

[6] E. Quartarone and P. Mustarelli, "Electrolytes for solid-state lithium rechargeable batteries: Recent advances and perspectives," Chem. Soc. Rev. **40**, 2525 (2011). https://doi.org/10.1039/C0CS00081G

[7] G. Wan, F. Guo, H. Li, Y. Cao, X. Ai, J. Qian, Y. Li, and H. Yang, "Suppression of dendritic lithium growth by in situ formation of a chemically stable and mechanically strong solid electrolyte interphase," ACS Appl. Mater. Interfaces **10**, 593 (2018). https://doi.org/10.1021/acsami.7b14662

[8] B. Wu, S. Wang, J. Lochala, D. Desrochers, B. Liu, W. Zhang, J. Yang, and J. Xiao, "The role of the solid electrolyte interphase layer in preventing Li dendrite growth in solid-state batteries," Energy Environ. Sci. **11**, 1803 (2018). https://doi.org/10.1039/C8EE00540K

[9] Z. Zhang, Y. Shao, B. Lotsch, Y.-S. Hu, H. Li, J. Janek, L. F. Nazar, C.-W. Nan, J. Maier, M. Armand, and L. Chen, "New horizons for inorganic solid state ion conductors," Energy Environ. Sci. **11**, 1945 (2018). https://doi.org/10.1039/C8EE01053F

[10] T. M. Bandhauer, S. Garimella, and T. F. Fuller, "A critical review of thermal issues in lithium-ion batteries," J. Electrochem. Soc. **158**, R1 (2011). https://doi.org/10.1149/1.3515880

[11] G. Liu, M. Ouyang, L. Lu, J. Li, and X. Han, "Analysis of the heat generation of lithium-ion battery during charging and discharging considering different influencing factors," J. Therm. Anal. Calorim. **116**, 1001 (2014). https://doi.org/10.1007/s10973-013-3599-9

[12] B. V. Lotsch and J. Maier, "Relevance of solid electrolytes for lithium-based batteries: A realistic view," J. Electroceram. **38**, 128 (2017). https://doi.org/10.1007/s10832-017-0091-0

[13] N. R. Abdulchalikova and A. É. Aliev, "Thermal properties of Li conducting superionic matirials," Synthetic Met. **71**, 1929 (1995). https://doi.org/10.1016/0379-6779(94)03112-J

[14] A. É. Aliev, V. F. Krivorotov, and P. K. Khabibullaev, "Specific heat and thermal conductivity of superionic conductors in the superionic phase," Phys. Solid State **39**, 1378 (1997). https://doi.org/10.1134/1.1130083

[15] Y. Cui, M. M. Mahmoud, M. Rohde, C. Ziebert, and H. J. Seifert, "Thermal and ionic conductivity studies of lithium aluminum germanium phosphate solid-state electrolyte," Solid State Ionics **289**, 125 (2016). https://doi.org/10.1016/j.ssi.2016.03.007

[16] A. A. El-Rahman, M. M. El-Desoky, and A. E.-W. El-Sharkawy, "Electrical and thermal properties of polycrystalline Li_2SO_4 and Ag_2SO_4," J. Phys. Chem. Solids **60**, 119 (1999). https://doi.org/10.1016/S0022-3697(98)00254-6

[17] L. S. Parfen'eva, A. I. Shelykh, I. A. Smirnov, A. V. Prokof'ev, W. Assmus, H. Misiorek, J. Mucha, A. Jezowski, and I. G. Vasil'eva, "Heat transport over nonmagnetic lithium chains in $LiCuVO_4$, a new one-dimensional superionic conductor," Phys. Solid State **45**, 2093 (2003). https://doi.org/10.1134/1.1626742

[18] H. Aono, E. Sugimoto, Y. Sadaoka, N. Imanaka, and G. y. Adachi, "Ionic conductivity of solid electrolytes based on lithium titanium phosphate," J. Electrochem. Soc. **137**, 1023 (1990). https://doi.org/10.1149/1.2086597

[19] M. A. Subramanian, R. Subramanian, and A. Clearfield, "Lithium ion conductors in the system $AB(IV)_2(PO_4)_3$ (B = Ti, Zr and Hf)," Solid State Ionics **18–19**, 562 (1986). https://doi.org/10.1016/0167-2738(86)90179-7

[20] A. Kubanska, L. Castro, L. Tortet, O. Schäf, M. Dollé, and R. Bouchet, "Elaboration of controlled size $Li_{1.5}Al_{0.5}Ge_{1.5}(PO_4)_3$ crystallites from glass-ceramics," Solid State Ionics **266**, 44 (2014). https://doi.org/10.1016/j.ssi.2014.07.013

[21] V. Thangadurai, A. K. Shukla, and J. Gopalakrishnan, "New lithium-ion conductors based on the NASICON structure," J. Mater. Chem. **9**, 739 (1999). https://doi.org/10.1039/A807007E

[22] J. C. Bachman, S. Muy, A. Grimaud, H.-H. Chang, N. Pour, S. F. Lux, O. Paschos, F. Maglia, S. Lupart, P. Lamp, L. Giordano, and Y. Shao-Horn, "Inorganic solid-state electrolytes for lithium batteries: Mechanisms and properties governing ion conduction," Chem. Rev. **116**, 140 (2016). https://doi.org/10.1021/acs.chemrev.5b00563

[23] I. Hanghofer, B. Gadermaier, A. Wilkening, D. Rettenwander, and H. M. R. Wilkening, "Lithium ion dynamics in $LiZr_2(PO_4)_3$ and $Li_{1.4}Ca_{0.2}Zr_{1.8}(PO_4)_3$," Dalton Trans. **48**, 9376 (2019). https://doi.org/10.1039/C9DT01786K

[24] H. Xie, Y. Li, and J. B. Goodenough, "NASICON-type $Li_{1+2x}Zr_{2-x}Ca_x(PO_4)_3$ with high ionic conductivity at room temperature," RSC Adv. **1**, 1728 (2011). https://doi.org/10.1039/C1RA00383F

[25] H. Xie, J. B. Goodenough, and Y. Li, "$Li_{1.2}Zr_{1.9}Ca_{0.1}(PO_4)_3$, a room-temperature Li-ion solid electrolyte," J. Power Sources **196**, 7760 (2011). https://doi.org/10.1016/j.jpowsour.2011.05.002

[26] Y. Li, M. Liu, K. Liu, and C.-A. Wang, "High Li^+ conduction in NASICON-type $Li_{1+x}Y_xZr_{2-x}(PO_4)_3$ at room temperature," J. Power Sources **240**, 50 (2013). https://doi.org/10.1016/j.jpowsour.2013.03.175

[27] J. Kuwano, N. Sato, M. Kato, and K. Takano, "Ionic conductivity of $LiM_2(PO_4)_3$ (M = Ti, Zr, Hf) and related compositions," Solid State Ionics **70–71**, 332 (1994). https://doi.org/10.1016/0167-2738(94)90332-8

[28] K. Arbi, M. Ayadi-Trabelsi, and J. Sanz, "Li mobility in triclinic and rhombohedral phases of the NASICON-type compound $LiZr_2(PO_4)_3$ as deduced from NMR spectroscopy," J. Mater. Chem. **12**, 2985 (2002). https://doi.org/10.1039/B203519G

[29] J. E. Iglesias and C. Pecharromán, "Room temperature triclinic modification of NASICON-type $LiZr_2(PO_4)_3$," Solid State Ionics **112**, 309 (1998). https://doi.org/10.1016/S0167-2738(98)00208-2

[30] V. I. Pet'kov, A. V. Markin, and N. N. Smirnova, "Thermodynamic properties of $LiZr_2(PO_4)_3$ crystal phosphate," Russ. J. Phys. Chem. A **87**, 1266 (2013). https://doi.org/10.1134/S0036024413070261

[31] M. Catti, A. Comotti, and S. Di Blas, "High-temperature lithium mobility in α-$LiZr_2(PO_4)_3$ NASICON by neutron diffraction," Chem. Mater. **15**, 1628 (2003). https://doi.org/10.1021/cm021374p

[32] M. Catti, S. Stramare, and R. Ibberson, "Lithium location in NASICON-type Li^+ conductors by neutron diffraction. I. Triclinic α'-$LiZr_2(PO_4)_3$," Solid State Ionics **123**, 173 (1999). https://doi.org/10.1016/S0167-2738(99)00089-2

[33] M. Catti, N. Morgante, and R. M. Ibberson, "Order–disorder and mobility of Li^+ in the β'- and β-$LiZr_2(PO_4)_3$ ionic conductors: A neutron diffraction study," J. Solid State Chem. **152**, 340 (2000). https://doi.org/10.1006/jssc.2000.8658

[34] Y. Ni, J. M. Hughes, and A. N. Mariano, "Crystal chemistry of the monazite and xenotime structures," Am. Mineral. **80**, 21 (1995). https://doi.org/10.2138/am-1995-1-203

[35] G. R. Levi and G. Peyronel, "Struttura cristallografica del gruppo isomorfo (Si^{4+}, Ti^{4+}, Zr^{4+}, Sn^{4+}, Hf^{4+}) P_2O_7," Z. Kristallogr. **92**, 190 (1935). https://doi.org/10.1524/zkri.1935.92.1.190

[36] H. Wang, S. Bai, L. Chen, A. Cuenat, G. Joshi, H. Kleinke, J. König, H. W. Lee, J. Martin, M.-W. Oh, W. D. Porter, Z. Ren, J. Salvador, J. Sharp, P. Taylor, A. J. Thompson, and Y. C. Tseng, "International round-robin study of the thermoelectric transport properties of an *n*-type half-Heusler compound from 300 K to 773 K," J. Electron. Mater. **44**, 4482 (2015). https://doi.org/10.1007/s11664-015-4006-z

[37] P. Hohenberg and W. Kohn, "Inhomogeneous electron gas," Phys. Rev. **136**, B864 (1964). https://doi.org/10.1103/PhysRev.136.B864

[38] W. Kohn and L. J. Sham, "Self-consistent equations including exchange and correlation effects," Phys. Rev. **140**, A1133 (1965). https://doi.org/10.1103/PhysRev.140.A1133

[39] G. Kresse and J. Hafner, "*Ab initio* molecular dynamics for liquid metals," Phys. Rev. B **47**, 558(R) (1993). https://doi.org/10.1103/PhysRevB.47.558

[40] T. D. Huan, "Pressure-stabilized binary compounds of magnesium and silicon," Phys. Rev. Materials **2**, 023803 (2018). https://doi.org/10.1103/PhysRevMaterials.2.023803

[41] M. H. Jacobs, "The structure of the metastable precipitates formed during ageing of an Al-Mg-Si alloy," Philos. Mag. **26**, 1 (1972). https://doi.org/10.1080/14786437208221015

[42] T. D. Huan, V. Sharma, G. A. Rossetti, and R. Ramprasad, "Pathways towards ferroelectricity in hafnia," Phys. Rev. B **90**, 064111 (2014). https://doi.org/10.1103/PhysRevB.90.064111

[43] T. S. Böscke, J. Müller, D. Bräuhaus, U. Schröder, and U. Böttger, "Ferroelectricity in hafnium oxide thin films," Appl. Phys. Lett. **99**, 102903 (2011). https://doi.org/10.1063/1.3634052

[44] R. Batra, T. D. Huan, G. A. Rossetti, and R. Ramprasad, "Dopants promoting ferroelectricity in hafnia: Insights from a comprehensive chemical space exploration," Chem. Mater. **29**, 9102 (2017). https://doi.org/10.1021/acs.chemmater.7b02835

[45] R. Batra, T. D. Huan, J. L. Jones, G. Rossetti, and R. Ramprasad, "Factors favoring ferroelectricity in hafnia: A first-principles computational study," J. Phys. Chem. C **121**, 4139 (2017). https://doi.org/10.1021/acs.jpcc.6b11972

[46] R. Batra, H. D. Tran, and R. Ramprasad, "Stabilization of metastable phases in hafnia owing to surface energy effects," Appl. Phys. Lett. **108**, 172902 (2016). https://doi.org/10.1063/1.4947490

[47] M. Aykol, S. S. Dwaraknath, W. Sun, and K. A. Persson, "Thermodynamic limit for synthesis of metastable inorganic materials," Sci. Adv. **4**, eaaq0148 (2018). https://doi.org/10.1126/sciadv.aaq0148

Supplementary Material for DOI: 10.1063/5.0013716

Thermal Transport in Phase-Stabilized Lithium Zirconate Phosphates

Sajad Yazdani,[1] Raana Kashfi-Sadabad,[2] Mayra Daniela Morales-Acosta,[3] Raul David Montaño,[4] Tuoc Ngoc Vu,[5] Huan Doan Tran,[6] Menghan Zhou,[7] Yufei Liu,[7] Jian He,[7] and Michael Thompson Pettes[8,a)]

[1] Department of Mechanical Engineering and Materials Science and Energy Sciences Institute, Yale University, New Haven, Connecticut 06511, USA
[2] School of Medicine, Stanford University, Stanford, California 94305, USA
[3] Institute of Materials Science, University of Connecticut, Storrs, Connecticut 06269, USA
[4] Department of Mechanical Engineering, The University of Texas at Austin, Austin, Texas 78712, USA
[5] Department of Theoretical Physics and Institute of Engineering Physics, Hanoi University of Science and Technology, Hanoi 10000, Vietnam
[6] School of Materials Science and Engineering, Georgia Institute of Technology, Atlanta, Georgia 30332, USA.
[7] Department of Physics and Astronomy, Clemson University, Clemson, South Carolina 29634, USA
[8] Center for Integrated Nanotechnologies (CINT), Materials Physics and Applications Division, Los Alamos National Laboratory, Los Alamos, New Mexico 87545, USA
[a)] Author to whom correspondence should be addressed: pettesmt@lanl.gov

1. Additional Experimental Details

Chemicals. Lithium carbonate (99.99% Li_2CO_3, 431559 Sigma-Aldrich), Yttrium(III) oxide (99.99% Y_2O_3, 205168 Sigma-Aldrich), Zirconium(IV) oxide (99.99% ZrO_2, 204994 Sigma-Aldrich) and Ammonium phosphate dibasic [99.99% $(NH4)_2HPO_4$, 379980 Sigma-Aldrich] were purchased from Sigma-Aldrich Co. LLC and used as received.

Synthesis of $Li_{1+x+y}Y_xZr_{2-x}(PO_4)_3$. Precursor amounts for the desired stoichiometry were weighed with a Mettler Toledo XP105DR analytical balance and mixed in a solid-state reaction, then fired in air at 1200 °C for 24 hours using an 18.4 L box furnace (BF51894C Moldatherm™ Lindberg/BlueM™, Thermo Electron Corp.). The fired powders were mechanically ground and

pressed at 1150 °C for 30 mins at 45 KPa using spark plasma sintering (SPS) in order to obtain solid pellets. Mass densities were measured by the Archimedes method similar to Ref. S1.

Structural and thermal characterizations. A Bruker D2 Phaser with Cu Kα radiation ($\lambda = 1.54056$ Å) and a high-speed linear detector, operated at 30 kV and 10 mA, was used to perform powder X-ray diffraction (XRD) measurements at room temperature. XRD patterns were collected using a standard Bragg-Brentano geometry over a 2θ range of 10 – 80°, with a scan speed of 2 sec/step and 0.01° increments. Quantitative determination of the crystallographic phase composition was obtained through Rietveld refinement of the XRD patterns using GSAS-II software[S2]. Thermal diffusivity (α) measurements were conducted on spark plasma sintered pellets with diameters of 12.7 mm via a NETZSCH laser flash LFA-457 from room temperature to 973 K. At each temperature three data points were collected. The low-temperature measurements of thermal conductivity (κ) from 30 to 312 K were carried out on polished rectangular bars using a custom designed apparatus described in Pope and Tritt *et al.*[S3], where the rectangular sample bars were cut by using a diamond saw from the same pellets used for laser flash measurements and precision fine-wire type-E thermocouples were used to measure temperature profiles (CHCO-001, Omega Engineering Inc.). Low-temperature differential scanning calorimetry (DSC) measurements were performed by the Thermoanalytical Section of the NETZSCH Instruments Testing Laboratory (Burlington, MA) using a NETZSCH model DSC 204 F1 from 78 to 473 K at 20 K min^{-1}. The DSC 204 F1 was operated in accordance with national and international standards (ASTM C351, D3417, D3418, D3895, D4565, E793, E794 and E1269 as well as DIN 51004, -51007, -53765, -65467, DIN EN 728, JIS R 1672 and ISO 10837, -11357, -11409). High-temperature DSC measurements (from 298 to 973 K at 20 Kmin^{-1}) were performed using a NETZSCH model DSC

404 F1 Pegasus® equipped with a Rh furnace. The system was vacuum-tight, and therefore samples were tested under pure inert, reducing or oxidizing atmospheres, as well as under vacuum.

2. Additional Structure Analysis

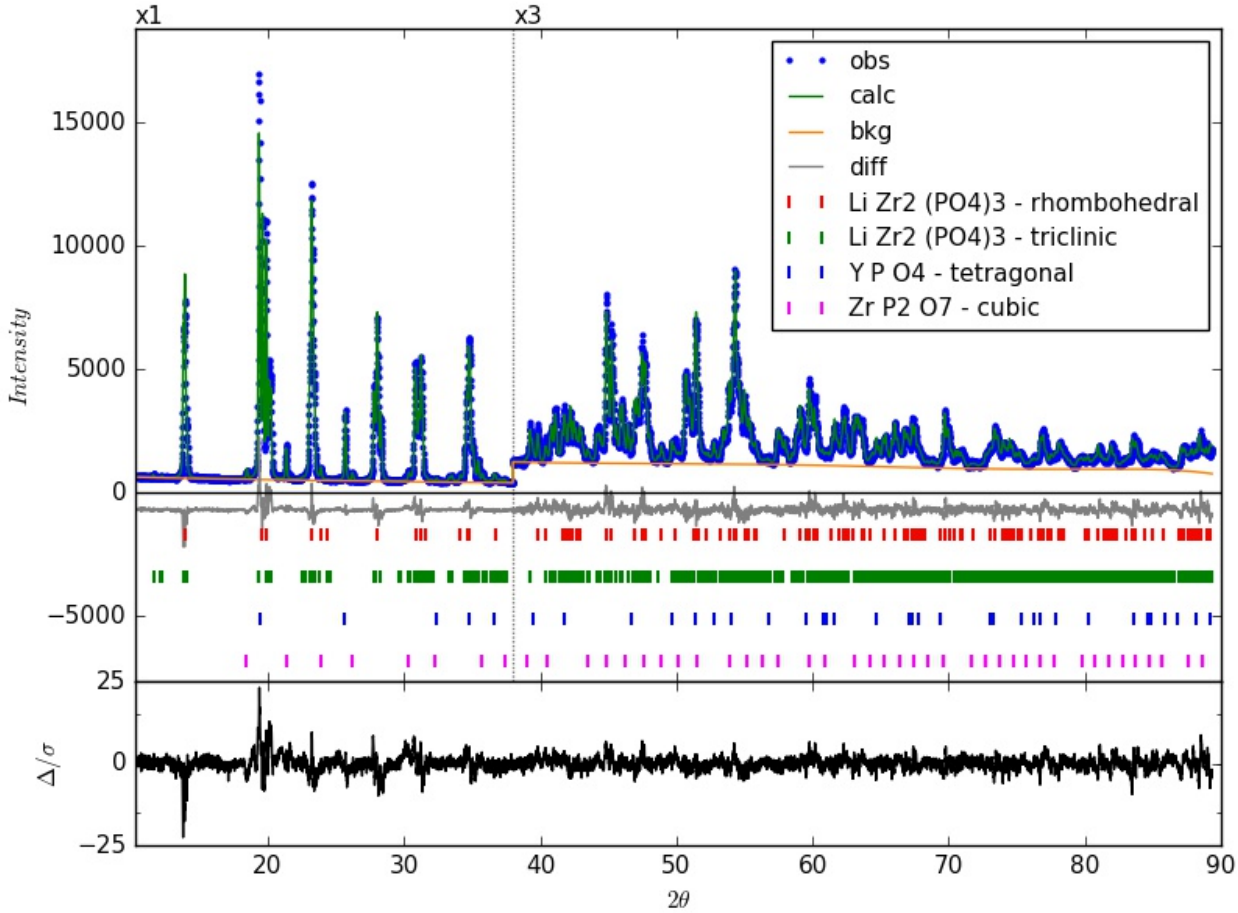

Fig. S1. *Rietveld refinement of the Li-deficient sample* $Li_{1+x+y}Y_xZr_{2-x}(PO_4)_3$ *(x = 0.15, y = - 0.2). In the upper panel, the blue dots represent the observed XRD data and the green solid line represents the calculated pattern. The vertical tick marks in the middle panel represent the peaks of the identified crystalline phases. The lower panel shows the difference between the observed and calculated diffraction patterns.*

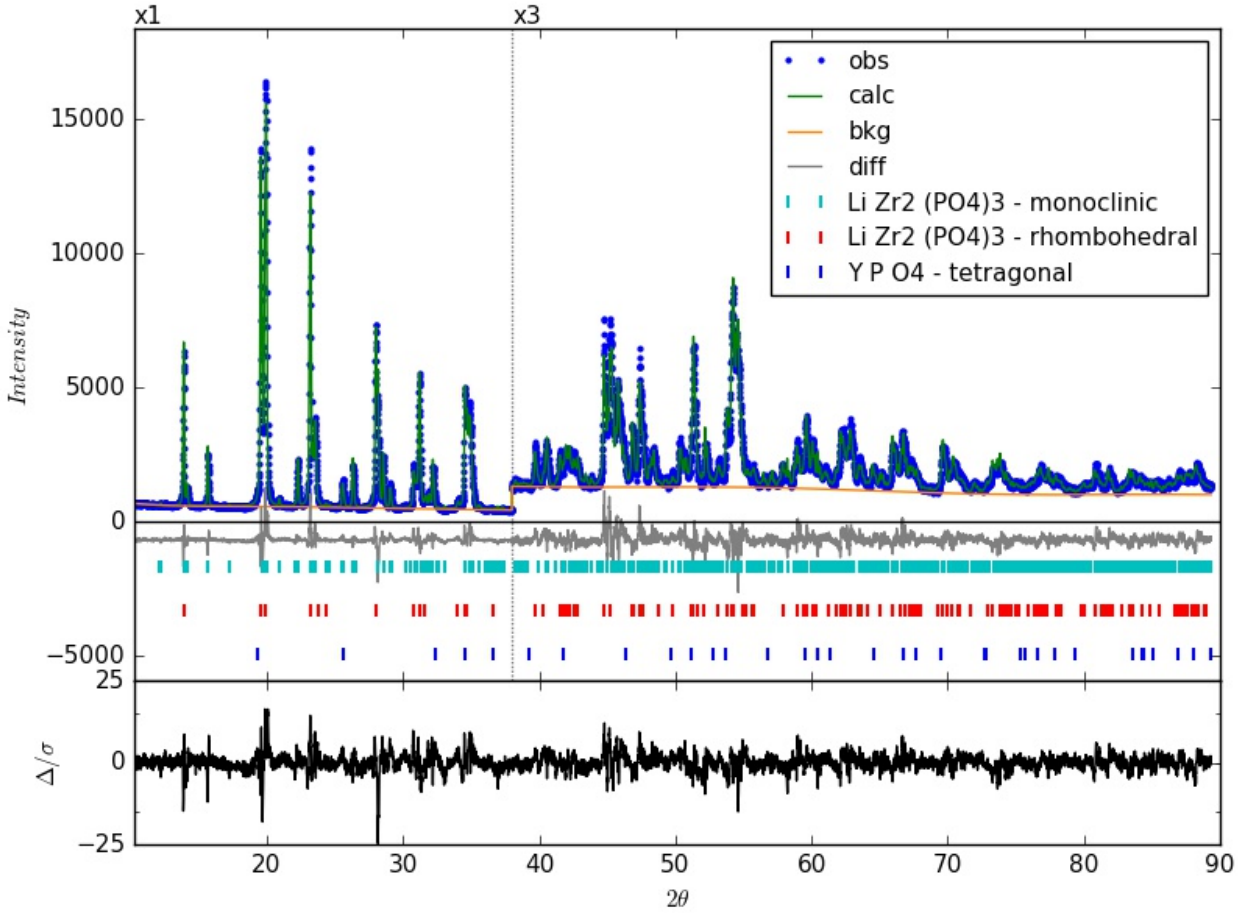

Fig. S2. *Rietveld refinement of the Li-excess sample* $Li_{1+x+y}Y_xZr_{2-x}(PO_4)_3$ *(x = 0.15, y = 0.2) sample. In the upper panel, the blue dots represent the observed XRD data and the green solid line represents the calculated pattern. The vertical tick marks in the middle panel represent the peaks of the identified crystalline phases. The lower panel shows the difference between the observed and calculated diffraction patterns.*

Table S1. *Lattice parameters and quantitative analysis obtained from the Rietveld refinement of the* $Li_{1+x+y}Y_xZr_{2-x}(PO_4)_3$ *(x = 0.15, -0.2 ≤ y ≤ 0.4 and x = 0.0, y = 0.0) samples. The weighted residual error (%) and chi squared are indicated by* R_w *and* χ^2*, respectively.*

	***x* = 0**	***x* = 0.15**			
	***y* = 0**	***y* = -0.2**	***y* = 0**	***y* = 0.2**	***y* = 0.4**
formula	**$LiZr_2(PO_4)_3$**				
SG & crystal sys.	**$R\bar{3}c$ (167), rhombohedral**				
***a* (Å)**	8.9218 (8)	8.9300 (3)	8.9386 (3)	8.9397 (4)	8.9372 (3)
***c* (Å)**	22.3555 (12)	22.3365 (3)	22.3315 (4)	22.3892 (6)	22.4066 (5)
weight (%)	12.9 (2)	36.5 (2)	97.5 (2)	55.9 (2)	69.1 (2)
formula	**$LiZr_2(PO_4)_3$**				
SG & crystal sys.	***P*$\bar{1}$ (2), triclinic**				
***a* (Å)**	15.1886 (18)	15.1908 (29)			
***b* (Å)**	8.9228 (1)	8.9256 (2)			
***c* (Å)**	9.1936 (7)	9.2007 (11)			
α (°)	89.6587 (7)	89.6589 (12)	—	—	—
β (°)	123.9113 (2)	123.8800 (30)			
γ (°)	90.4300 (2)	90.4016 (32)			
weight (%)	86.8 (2)	55.5 (2)			
formula	**YPO_4**				
SG & crystal sys.	***I*4$_1$/*amd* (141), tetragonal**				
***a* (Å)**		6.9372 (2)	6.9365 (7)	6.9322 (20)	6.9371 (19)
***c* (Å)**	—	6.0679 (5)	6.1119 (18)	6.1246 (40)	6.0016 (39)
weight (%)		5.4 (1)	2.5 (1)	0.5 (1)	0.6 (1)
formula	**ZrP_2O_7**				
SG & crystal sys.	***Pa*$\bar{3}$ (205), cubic**				
***a* (Å)**	8.2063 (46)	8.3243 (4)	—	—	—
weight (%)	0.3 (1)	2.5 (1)			
formula	**$LiZr_2(PO_4)_3$**				
SG & crystal sys.	***P*2$_1$/*c* (14), monoclinic**				
***a* (Å)**				8.8913 (2)	8.8775 (7)
***b* (Å)**				9.0218 (2)	9.0134 (7)
***c* (Å)**	—	—	—	12.4965 (3)	12.4897 (8)
β (°)				90.1788 (25)	89.8810 (17)
weight (%)				43.6 (2)	30.3 (2)
R_w (%)	8.90	7.851	10.786	9.105	10.293
χ^2	2.76	2.32	3.15	2.63	2.97

Table S2. *Ab initio calculated lattice parameters of the rhombohedral and triclinic phases of lithium zirconate phosphate,* $LiZr_2(PO_4)_3$.

phase	*unit* cell parameters					
	a **(Å)**	***b*** **(Å)**	***c*** **(Å)**	α **(°)**	β **(°)**	γ **(°)**
rhombohedral	8.91	8.91	22.11	90	90	120
triclinic	8.82	8.87	9.22	90.72	118.62	118.98

3. Thermal Analysis of Pure $LiZr_2(PO_4)_3$

The DSC analysis, α, and κ measurements of the material with no Y^{3+} substitution ($x = 0$, $y = 0$) are shown in Fig. S3. Both low and high-temperature DSC measurements showed a phase change in the range from 300 to 345 K with features at ~318 and 329 K [Fig. S3(a,b)]. This phase transformation caused an anomaly in the obtained α and, consequently, in κ as depicted in the shaded area of Fig. S3(c,d). The κ approached 0.72 W m^{-1} K^{-1} at 973 K, close to those obtained for the rest of the samples.

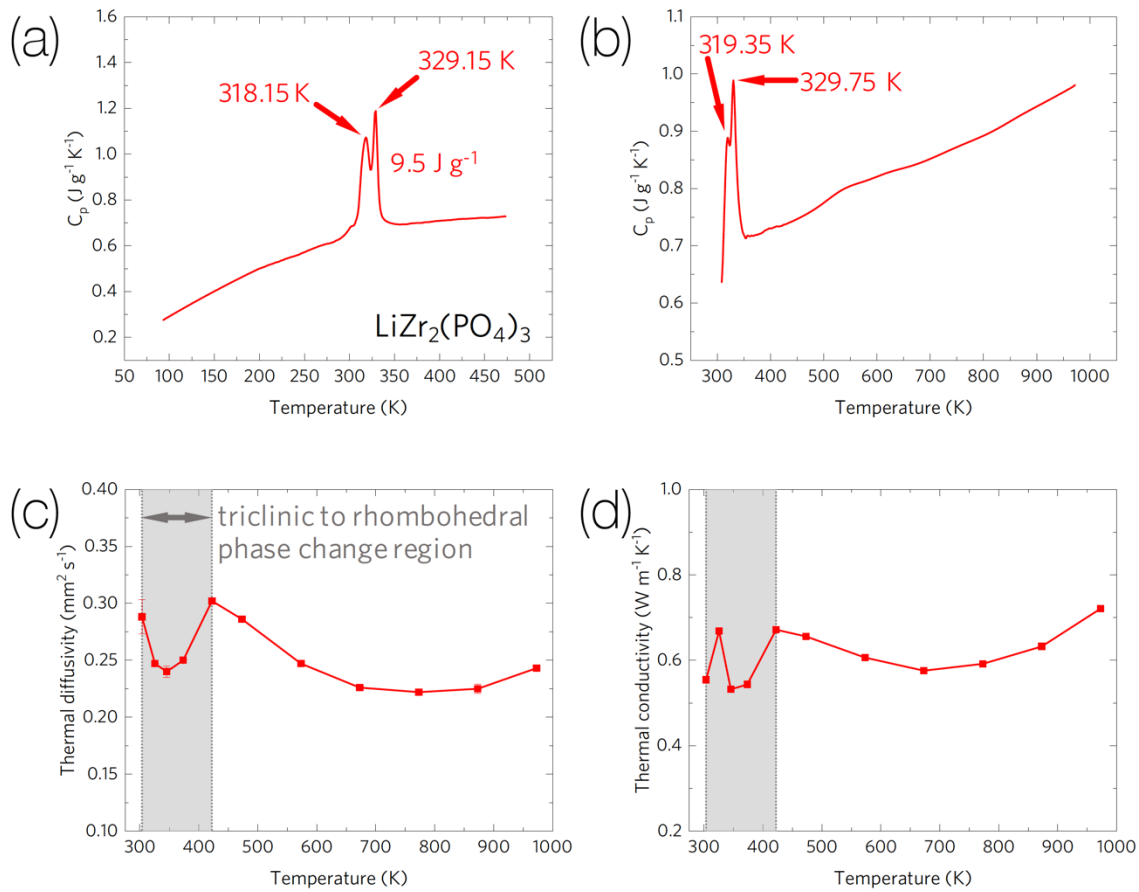

Fig. S3. *Thermal properties of pure lithium zirconate phosphate.* (a) Low- and (b) high-temperature specific heat, c_p, (c) thermal diffusivity, and (d) thermal conductivity for pure $LiZr_2(PO_4)_3$.

4. Additional Theoretical Analysis Concerning Rhombohedral Phase Stabilization

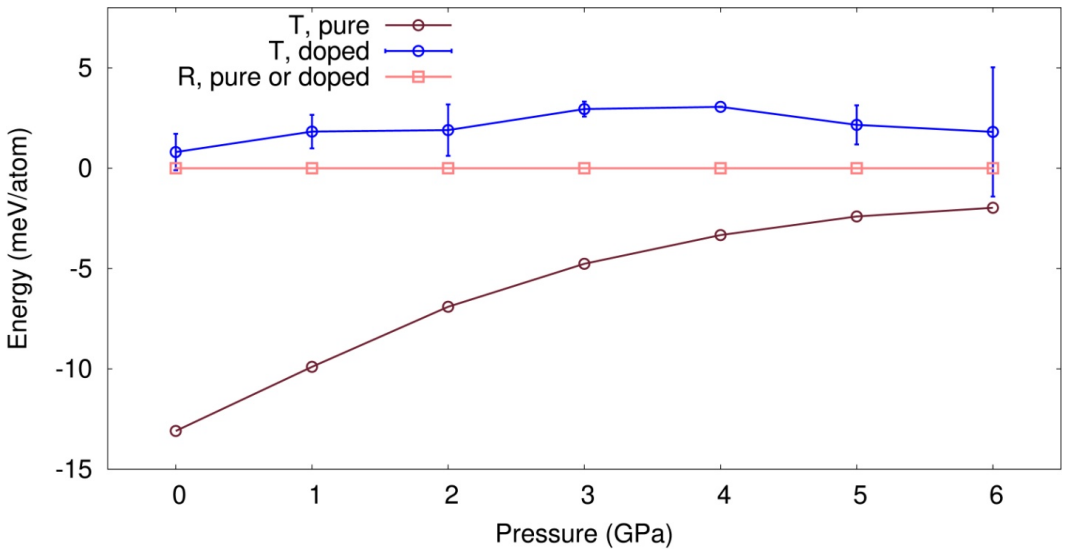

Fig. S4. *Ab initio phase stability of yttrium-doped lithium zirconate phosphate. Relative energy computed for the triclinic phase (T) with respect to that of the rhombohedral phase (R). The error bar of the doped triclinic phase originates from calculations of two different sites of Zr that are substituted by Y.*

The crystallographic information files developed in the *ab initio* calculations in this work are given below.

4.1 LZP_rhombohedral_pure

```
#======================================================================
# CRYSTAL DATA
#----------------------------------------------------------------------
data_VESTA_phase_1

_chemical_name_common                   'findsym-output'
_cell_length_a                          8.90832
_cell_length_b                          8.90832
_cell_length_c                          22.10688
_cell_angle_alpha                       90
_cell_angle_beta                        90
_cell_angle_gamma                       120
_space_group_name_H-M_alt               'R -3 c'
_space_group_IT_number                  167

loop_
_space_group_symop_operation_xyz
   'x, y, z'
```

```
   '-x, -y, -z'
   '-y, x-y, z'
   'y, -x+y, -z'
   '-x+y, -x, z'
   'x-y, x, -z'
   'y, x, -z+1/2'
   '-y, -x, z+1/2'
   'x-y, -y, -z+1/2'
   '-x+y, y, z+1/2'
   '-x, -x+y, -z+1/2'
   'x, x-y, z+1/2'
   'x+2/3, y+1/3, z+1/3'
   '-x+2/3, -y+1/3, -z+1/3'
   '-y+2/3, x-y+1/3, z+1/3'
   'y+2/3, -x+y+1/3, -z+1/3'
   '-x+y+2/3, -x+1/3, z+1/3'
   'x-y+2/3, x+1/3, -z+1/3'
   'y+2/3, x+1/3, -z+5/6'
   '-y+2/3, -x+1/3, z+5/6'
   'x-y+2/3, -y+1/3, -z+5/6'
   '-x+y+2/3, y+1/3, z+5/6'
   '-x+2/3, -x+y+1/3, -z+5/6'
   'x+2/3, x-y+1/3, z+5/6'
   'x+1/3, y+2/3, z+2/3'
   '-x+1/3, -y+2/3, -z+2/3'
   '-y+1/3, x-y+2/3, z+2/3'
   'y+1/3, -x+y+2/3, -z+2/3'
   '-x+y+1/3, -x+2/3, z+2/3'
   'x-y+1/3, x+2/3, -z+2/3'
   'y+1/3, x+2/3, -z+1/6'
   '-y+1/3, -x+2/3, z+1/6'
   'x-y+1/3, -y+2/3, -z+1/6'
   '-x+y+1/3, y+2/3, z+1/6'
   '-x+1/3, -x+y+2/3, -z+1/6'
   'x+1/3, x-y+2/3, z+1/6'

loop_
   _atom_site_label
   _atom_site_occupancy
   _atom_site_fract_x
   _atom_site_fract_y
   _atom_site_fract_z
   _atom_site_adp_type
   _atom_site_B_iso_or_equiv
   _atom_site_type_symbol
   A1         1.0     0.000000      0.000000      0.000000     Biso  1.000000 Li
   B1         1.0     0.000000      0.000000      0.642630     Biso  1.000000 Zr
   C1         1.0     0.293440      0.000000      0.250000     Biso  1.000000 P
   D1         1.0     0.473410      0.333333      0.026440     Biso  1.000000 O
   D2         1.0     0.312140      0.836430      0.247240     Biso  1.000000 O
```

4.2 LZP_rhombohedral_Y-doped

```
#======================================================================
# CRYSTAL DATA
#----------------------------------------------------------------------
data_VESTA_phase_1

_chemical_name_common                  'contcar-rhombohedral_expr_doped       '
_cell_length_a                         18.21837
_cell_length_b                         9.09368
_cell_length_c                         9.07644
_cell_angle_alpha                      59.69571
_cell_angle_beta                       59.54736
_cell_angle_gamma                      59.47446
_space_group_name_H-M_alt              'P 1'
_space_group_IT_number                 1

loop_
_space_group_symop_operation_xyz
```

```
   'x, y, z'

loop_
   _atom_site_label
   _atom_site_occupancy
   _atom_site_fract_x
   _atom_site_fract_y
   _atom_site_fract_z
   _atom_site_adp_type
   _atom_site_B_iso_or_equiv
   _atom_site_type_symbol
   Li1        1.0     0.916572      0.055604      0.159505     Biso  1.000000 Li
   Li2        1.0     0.188381      0.632153      0.520203     Biso  1.000000 Li
   Li3        1.0     0.527921      0.150468      0.839852     Biso  1.000000 Li
   Li4        1.0     0.771603      0.334438      0.677705     Biso  1.000000 Li
   Zr1        1.0     0.324020      0.635378      0.638626     Biso  1.000000 Zr
   Zr2        1.0     0.433979      0.847699      0.859740     Biso  1.000000 Zr
   Zr3        1.0     0.068301      0.146830      0.138870     Biso  1.000000 Zr
   Zr4        1.0     0.822979      0.642875      0.635917     Biso  1.000000 Zr
   Zr5        1.0     0.681046      0.364406      0.357705     Biso  1.000000 Zr
   Zr6        1.0     0.931062      0.859550      0.858230     Biso  1.000000 Zr
   Zr7        1.0     0.575454      0.133607      0.143713     Biso  1.000000 Zr
   Y1         1.0     0.179486      0.364728      0.350127     Biso  1.000000 Y
   P1         1.0     0.263700      0.946066      0.257641     Biso  1.000000 P
   P2         1.0     0.233546      0.023005      0.755146     Biso  1.000000 P
   P3         1.0     0.130409      0.533451      0.941306     Biso  1.000000 P
   P4         1.0     0.384556      0.448631      0.025791     Biso  1.000000 P
   P5         1.0     0.488428      0.240659      0.541466     Biso  1.000000 P
   P6         1.0     0.013329      0.762489      0.453638     Biso  1.000000 P
   P7         1.0     0.773877      0.965239      0.249589     Biso  1.000000 P
   P8         1.0     0.733862      0.042895      0.749347     Biso  1.000000 P
   P9         1.0     0.627490      0.527517      0.961562     Biso  1.000000 P
   P10        1.0     0.873278      0.468393      0.033377     Biso  1.000000 P
   P11        1.0     0.976772      0.254295      0.536861     Biso  1.000000 P
   P12        1.0     0.516740      0.755076      0.459953     Biso  1.000000 P
   O1         1.0     0.432267      0.727517      0.492946     Biso  1.000000 O
   O2         1.0     0.049949      0.311381      0.504896     Biso  1.000000 O
   O3         1.0     0.247346      0.862768      0.715451     Biso  1.000000 O
   O4         1.0     0.250122      0.102637      0.297954     Biso  1.000000 O
   O5         1.0     0.360196      0.484912      0.866810     Biso  1.000000 O
   O6         1.0     0.154386      0.511407      0.089938     Biso  1.000000 O
   O7         1.0     0.983382      0.817298      0.616402     Biso  1.000000 O
   O8         1.0     0.510074      0.195087      0.378648     Biso  1.000000 O
   O9         1.0     0.410550      0.606561      0.982545     Biso  1.000000 O
   O10        1.0     0.105670      0.369983      0.990633     Biso  1.000000 O
   O11        1.0     0.316537      0.982556      0.793259     Biso  1.000000 O
   O12        1.0     0.179467      0.983902      0.222993     Biso  1.000000 O
   O13        1.0     0.405737      0.414032      0.548255     Biso  1.000000 O
   O14        1.0     0.109692      0.621401      0.433176     Biso  1.000000 O
   O15        1.0     0.272721      0.765487      0.420383     Biso  1.000000 O
   O16        1.0     0.219160      0.202683      0.599904     Biso  1.000000 O
   O17        1.0     0.209653      0.549204      0.755786     Biso  1.000000 O
   O18        1.0     0.307565      0.425592      0.205884     Biso  1.000000 O
   O19        1.0     0.469743      0.086304      0.726181     Biso  1.000000 O
   O20        1.0     0.011604      0.932550      0.278672     Biso  1.000000 O
   O21        1.0     0.048920      0.709031      0.909238     Biso  1.000000 O
   O22        1.0     0.468785      0.270494      0.033712     Biso  1.000000 O
   O23        1.0     0.349664      0.917096      0.092081     Biso  1.000000 O
   O24        1.0     0.147464      0.046289      0.923667     Biso  1.000000 O
   O25        1.0     0.944197      0.689806      0.485366     Biso  1.000000 O
   O26        1.0     0.571287      0.262847      0.527469     Biso  1.000000 O
   O27        1.0     0.762758      0.880839      0.696392     Biso  1.000000 O
   O28        1.0     0.765650      0.122686      0.287489     Biso  1.000000 O
   O29        1.0     0.853816      0.502332      0.870598     Biso  1.000000 O
   O30        1.0     0.645845      0.483273      0.130470     Biso  1.000000 O
   O31        1.0     0.503290      0.797087      0.617897     Biso  1.000000 O
   O32        1.0     0.996773      0.212952      0.371698     Biso  1.000000 O
   O33        1.0     0.898381      0.623447      0.997649     Biso  1.000000 O
   O34        1.0     0.606222      0.370888      0.986483     Biso  1.000000 O
   O35        1.0     0.803131      0.028014      0.810765     Biso  1.000000 O
   O36        1.0     0.696096      0.012551      0.192803     Biso  1.000000 O
```

```
   O37        1.0     0.881114      0.405704      0.567744     Biso  1.000000 O
   O38        1.0     0.600143      0.582047      0.443272     Biso  1.000000 O
   O39        1.0     0.776678      0.794062      0.418230     Biso  1.000000 O
   O40        1.0     0.725118      0.225081      0.587675     Biso  1.000000 O
   O41        1.0     0.712759      0.541040      0.788194     Biso  1.000000 O
   O42        1.0     0.789886      0.452323      0.207332     Biso  1.000000 O
   O43        1.0     0.967278      0.087389      0.710385     Biso  1.000000 O
   O44        1.0     0.535848      0.911514      0.281379     Biso  1.000000 O
   O45        1.0     0.549119      0.708302      0.934471     Biso  1.000000 O
   O46        1.0     0.950307      0.280869      0.063902     Biso  1.000000 O
   O47        1.0     0.867142      0.933588      0.094993     Biso  1.000000 O
   O48        1.0     0.639787      0.059733      0.902062     Biso  1.000000 O
```

4.3 LZP_triclinic_pure

```
#======================================================================
# CRYSTAL DATA
#----------------------------------------------------------------------
data_VESTA_phase_1

_chemical_name_common                   'findsym-output'
_cell_length_a                          8.82426
_cell_length_b                          8.87228
_cell_length_c                          9.21555
_cell_angle_alpha                       118.61647
_cell_angle_beta                        90.72206
_cell_angle_gamma                       118.98489
_space_group_name_H-M_alt               'P -1'
_space_group_IT_number                  2

loop_
_space_group_symop_operation_xyz
   'x, y, z'
   '-x, -y, -z'

loop_
   _atom_site_label
   _atom_site_occupancy
   _atom_site_fract_x
   _atom_site_fract_y
   _atom_site_fract_z
   _atom_site_adp_type
   _atom_site_B_iso_or_equiv
   _atom_site_type_symbol
   A1         1.0     0.258190      0.306260      0.610190     Biso  1.000000 Li
   B1         1.0     0.135280      0.290500     -0.064140     Biso  1.000000 Zr
   B2         1.0     0.358070      0.717640      0.572280     Biso  1.000000 Zr
   C1         1.0     0.042650      0.507430      0.754470     Biso  1.000000 P
   C2         1.0     0.247000      0.216880      0.261060     Biso  1.000000 P
   C3         1.0     0.468000      0.225790      0.746900     Biso  1.000000 P
   D1         1.0     0.028670      0.630900     -0.065480     Biso  1.000000 O
   D2         1.0     0.194890      0.658210      0.719390     Biso  1.000000 O
   D3         1.0     0.095140      0.361700      0.750960     Biso  1.000000 O
   D4         1.0     0.269490      0.392940      0.440140     Biso  1.000000 O
   D5         1.0     0.088840      0.011230      0.230150     Biso  1.000000 O
   D6         1.0     0.292760      0.213710      0.783340     Biso  1.000000 O
   D7         1.0     0.141590      0.623510      0.387650     Biso  1.000000 O
   D8         1.0     0.425180      0.223730      0.269150     Biso  1.000000 O
   D9         1.0     0.479610      0.262910      0.597110     Biso  1.000000 O
   D10        1.0     0.636570      0.404770     -0.091430     Biso  1.000000 O
   D11        1.0     0.796910      0.762400      0.888020     Biso  1.000000 O
   D12        1.0     0.446890      0.020610      0.688120     Biso  1.000000 O
```

4.4 LZP_triclinic_Y-doped (configuration 1 of 2)

```
#======================================================================
# CRYSTAL DATA
#----------------------------------------------------------------------
```

```
data_VESTA_phase_1

_chemical_name_common                   'CONTCAR-triclinic_expr_doped          '
_cell_length_a                          20.464649
_cell_length_b                          8.919940
_cell_length_c                          8.854630
_cell_angle_alpha                       60.884918
_cell_angle_beta                        49.819550
_cell_angle_gamma                       65.265327
_cell_volume                            1065.581081
_space_group_name_H-M_alt               'P 1'
_space_group_IT_number                  1

loop_
_space_group_symop_operation_xyz
   'x, y, z'

loop_
   _atom_site_label
   _atom_site_occupancy
   _atom_site_fract_x
   _atom_site_fract_y
   _atom_site_fract_z
   _atom_site_adp_type
   _atom_site_B_iso_or_equiv
   _atom_site_type_symbol
   Li1         1.0     0.309272     0.988901     0.646305    Biso  1.000000 Li
   Li2         1.0     0.804909     0.500298     0.645613    Biso  1.000000 Li
   Li3         1.0     0.193294     0.517064     0.342987    Biso  1.000000 Li
   Li4         1.0     0.692194     0.006995     0.350972    Biso  1.000000 Li
   Zr1         1.0     0.469399     0.176333     0.198797    Biso  1.000000 Zr
   Zr2         1.0     0.969235     0.677651     0.195974    Biso  1.000000 Zr
   Zr3         1.0     0.028002     0.324279     0.803615    Biso  1.000000 Zr
   Zr4         1.0     0.536207     0.819043     0.797817    Biso  1.000000 Zr
   Zr5         1.0     0.786366     0.068583     0.785289    Biso  1.000000 Zr
   Zr6         1.0     0.215395     0.935832     0.210801    Biso  1.000000 Zr
   Zr7         1.0     0.714364     0.431565     0.213639    Biso  1.000000 Zr
   Y1          1.0     0.285981     0.563224     0.789278    Biso  1.000000 Y
   P1          1.0     0.379050     0.876144     0.279432    Biso  1.000000 P
   P2          1.0     0.875872     0.373538     0.289212    Biso  1.000000 P
   P3          1.0     0.121398     0.630396     0.706538    Biso  1.000000 P
   P4          1.0     0.624024     0.131553     0.709952    Biso  1.000000 P
   P5          1.0     0.129198     0.917374     0.987094    Biso  1.000000 P
   P6          1.0     0.631489     0.410418     0.988419    Biso  1.000000 P
   P7          1.0     0.372072     0.587878     0.019293    Biso  1.000000 P
   P8          1.0     0.867510     0.085240     0.018942    Biso  1.000000 P
   P9          1.0     0.376488     0.136085     0.720436    Biso  1.000000 P
   P10         1.0     0.872032     0.649259     0.719953    Biso  1.000000 P
   P11         1.0     0.123274     0.349386     0.287097    Biso  1.000000 P
   P12         1.0     0.627312     0.850568     0.278045    Biso  1.000000 P
   O1          1.0     0.468716     0.853315     0.079962    Biso  1.000000 O
   O2          1.0     0.964683     0.340805     0.095436    Biso  1.000000 O
   O3          1.0     0.032806     0.668210     0.901018    Biso  1.000000 O
   O4          1.0     0.535239     0.165540     0.904175    Biso  1.000000 O
   O5          1.0     0.364048     0.705218     0.455902    Biso  1.000000 O
   O6          1.0     0.858828     0.206476     0.477546    Biso  1.000000 O
   O7          1.0     0.141044     0.800572     0.519473    Biso  1.000000 O
   O8          1.0     0.640807     0.299399     0.523216    Biso  1.000000 O
   O9          1.0     0.377083     0.017480     0.338551    Biso  1.000000 O
   O10         1.0     0.874621     0.518172     0.341948    Biso  1.000000 O
   O11         1.0     0.117769     0.495913     0.647697    Biso  1.000000 O
   O12         1.0     0.625022     0.988474     0.655140    Biso  1.000000 O
   O13         1.0     0.217863     0.841237     0.823134    Biso  1.000000 O
   O14         1.0     0.720224     0.325057     0.831482    Biso  1.000000 O
   O15         1.0     0.282453     0.672018     0.177745    Biso  1.000000 O
   O16         1.0     0.778075     0.170413     0.174944    Biso  1.000000 O
   O17         1.0     0.107963     0.108989     0.875182    Biso  1.000000 O
   O18         1.0     0.617102     0.601199     0.861771    Biso  1.000000 O
   O19         1.0     0.386324     0.395335     0.142685    Biso  1.000000 O
   O20         1.0     0.885299     0.896159     0.142928    Biso  1.000000 O
   O21         1.0     0.392787     0.171501     0.509170    Biso  1.000000 O
```

```
   O22         1.0     0.891813     0.675461     0.508410    Biso  1.000000 O
   O23         1.0     0.096351     0.303999     0.510943    Biso  1.000000 O
   O24         1.0     0.610969     0.818619     0.488008    Biso  1.000000 O
   O25         1.0     0.192358     0.559618     0.746466    Biso  1.000000 O
   O26         1.0     0.695171     0.072038     0.750064    Biso  1.000000 O
   O27         1.0     0.307400     0.939243     0.238446    Biso  1.000000 O
   O28         1.0     0.804616     0.430217     0.249478    Biso  1.000000 O
   O29         1.0     0.137181     0.906192     0.155118    Biso  1.000000 O
   O30         1.0     0.635677     0.405983     0.158487    Biso  1.000000 O
   O31         1.0     0.368282     0.604278     0.844997    Biso  1.000000 O
   O32         1.0     0.863543     0.086102     0.849991    Biso  1.000000 O
   O33         1.0     0.302802     0.021514     0.880404    Biso  1.000000 O
   O34         1.0     0.796922     0.538719     0.882657    Biso  1.000000 O
   O35         1.0     0.195865     0.461126     0.145364    Biso  1.000000 O
   O36         1.0     0.701460     0.962926     0.115427    Biso  1.000000 O
   O37         1.0     0.459339     0.034893     0.715686    Biso  1.000000 O
   O38         1.0     0.951030     0.551652     0.731791    Biso  1.000000 O
   O39         1.0     0.045726     0.450514     0.267435    Biso  1.000000 O
   O40         1.0     0.546444     0.949141     0.273450    Biso  1.000000 O
   O41         1.0     0.446760     0.675248     0.925989    Biso  1.000000 O
   O42         1.0     0.939390     0.184576     0.916063    Biso  1.000000 O
   O43         1.0     0.056332     0.817683     0.093188    Biso  1.000000 O
   O44         1.0     0.557017     0.317022     0.092568    Biso  1.000000 O
   O45         1.0     0.349253     0.302854     0.766315    Biso  1.000000 O
   O46         1.0     0.843211     0.826124     0.753266    Biso  1.000000 O
   O47         1.0     0.156409     0.179125     0.234565    Biso  1.000000 O
   O48         1.0     0.655776     0.675815     0.240821    Biso  1.000000 O
```

4.5 LZP_triclinic_Y-doped (configuration 2 of 2)

```
#======================================================================
# CRYSTAL DATA
#----------------------------------------------------------------------
data_VESTA_phase_1

_chemical_name_common                  'CONTCAR-triclinic_expr_doped1         '
_cell_length_a                         20.408911
_cell_length_b                         8.899260
_cell_length_c                         8.867820
_cell_angle_alpha                      61.174931
_cell_angle_beta                       49.843819
_cell_angle_gamma                      65.337646
_cell_volume                           1064.759695
_space_group_name_H-M_alt              'P 1'
_space_group_IT_number                 1

loop_
_space_group_symop_operation_xyz
   'x, y, z'

loop_
   _atom_site_label
   _atom_site_occupancy
   _atom_site_fract_x
   _atom_site_fract_y
   _atom_site_fract_z
   _atom_site_adp_type
   _atom_site_B_iso_or_equiv
   _atom_site_type_symbol
   Li1         1.0     0.291427     0.024287     0.645677    Biso  1.000000 Li
   Li2         1.0     0.805999     0.495189     0.650051    Biso  1.000000 Li
   Li3         1.0     0.191983     0.508049     0.349689    Biso  1.000000 Li
   Li4         1.0     0.690140     0.006494     0.353796    Biso  1.000000 Li
   Zr1         1.0     0.467874     0.175226     0.200992    Biso  1.000000 Zr
   Zr2         1.0     0.969428     0.677632     0.195236    Biso  1.000000 Zr
   Zr3         1.0     0.531337     0.821548     0.801042    Biso  1.000000 Zr
   Zr4         1.0     0.291535     0.566114     0.776564    Biso  1.000000 Zr
   Zr5         1.0     0.781312     0.069082     0.793489    Biso  1.000000 Zr
   Zr6         1.0     0.214472     0.931101     0.214335    Biso  1.000000 Zr
   Zr7         1.0     0.715951     0.429728     0.212678    Biso  1.000000 Zr
```

Y1	1.0	0.035005	0.319979	0.802234	Biso	1.000000	Y
P1	1.0	0.377954	0.872553	0.284700	Biso	1.000000	P
P2	1.0	0.876007	0.370311	0.296063	Biso	1.000000	P
P3	1.0	0.127429	0.635642	0.702531	Biso	1.000000	P
P4	1.0	0.620667	0.133505	0.711721	Biso	1.000000	P
P5	1.0	0.134892	0.905031	0.986790	Biso	1.000000	P
P6	1.0	0.628513	0.413375	0.992673	Biso	1.000000	P
P7	1.0	0.370087	0.583457	0.016819	Biso	1.000000	P
P8	1.0	0.867311	0.082112	0.019187	Biso	1.000000	P
P9	1.0	0.373164	0.144336	0.719838	Biso	1.000000	P
P10	1.0	0.873178	0.650645	0.719247	Biso	1.000000	P
P11	1.0	0.129594	0.352891	0.268473	Biso	1.000000	P
P12	1.0	0.624393	0.849484	0.282229	Biso	1.000000	P
O1	1.0	0.467423	0.843054	0.089189	Biso	1.000000	O
O2	1.0	0.966249	0.327445	0.115572	Biso	1.000000	O
O3	1.0	0.037865	0.659633	0.903296	Biso	1.000000	O
O4	1.0	0.531488	0.170325	0.904372	Biso	1.000000	O
O5	1.0	0.363581	0.704641	0.468608	Biso	1.000000	O
O6	1.0	0.853239	0.208800	0.491020	Biso	1.000000	O
O7	1.0	0.140630	0.810451	0.526288	Biso	1.000000	O
O8	1.0	0.640198	0.298924	0.522587	Biso	1.000000	O
O9	1.0	0.373775	0.019456	0.339803	Biso	1.000000	O
O10	1.0	0.873390	0.518615	0.347597	Biso	1.000000	O
O11	1.0	0.132481	0.497866	0.636587	Biso	1.000000	O
O12	1.0	0.621140	0.989558	0.658298	Biso	1.000000	O
O13	1.0	0.223894	0.813316	0.835739	Biso	1.000000	O
O14	1.0	0.717676	0.327636	0.836242	Biso	1.000000	O
O15	1.0	0.280834	0.672277	0.169116	Biso	1.000000	O
O16	1.0	0.777263	0.168494	0.175829	Biso	1.000000	O
O17	1.0	0.130752	0.094901	0.852272	Biso	1.000000	O
O18	1.0	0.611324	0.601479	0.866583	Biso	1.000000	O
O19	1.0	0.385590	0.395927	0.146291	Biso	1.000000	O
O20	1.0	0.883893	0.892321	0.145991	Biso	1.000000	O
O21	1.0	0.389961	0.171437	0.511786	Biso	1.000000	O
O22	1.0	0.893215	0.675549	0.507663	Biso	1.000000	O
O23	1.0	0.115769	0.327259	0.470783	Biso	1.000000	O
O24	1.0	0.605571	0.821097	0.493168	Biso	1.000000	O
O25	1.0	0.199192	0.578452	0.740941	Biso	1.000000	O
O26	1.0	0.690805	0.072408	0.755782	Biso	1.000000	O
O27	1.0	0.306670	0.927068	0.245552	Biso	1.000000	O
O28	1.0	0.806614	0.427444	0.248836	Biso	1.000000	O
O29	1.0	0.136626	0.891127	0.165248	Biso	1.000000	O
O30	1.0	0.634382	0.414230	0.157252	Biso	1.000000	O
O31	1.0	0.367476	0.579838	0.848617	Biso	1.000000	O
O32	1.0	0.859995	0.076449	0.858607	Biso	1.000000	O
O33	1.0	0.296598	0.038570	0.885684	Biso	1.000000	O
O34	1.0	0.799633	0.535213	0.881648	Biso	1.000000	O
O35	1.0	0.204983	0.461357	0.099019	Biso	1.000000	O
O36	1.0	0.697460	0.964338	0.122780	Biso	1.000000	O
O37	1.0	0.453410	0.044473	0.726975	Biso	1.000000	O
O38	1.0	0.953593	0.565662	0.724278	Biso	1.000000	O
O39	1.0	0.047485	0.452779	0.267488	Biso	1.000000	O
O40	1.0	0.544149	0.945248	0.273257	Biso	1.000000	O
O41	1.0	0.443850	0.679918	0.911431	Biso	1.000000	O
O42	1.0	0.940063	0.178842	0.909314	Biso	1.000000	O
O43	1.0	0.057649	0.822622	0.082800	Biso	1.000000	O
O44	1.0	0.555082	0.313998	0.101383	Biso	1.000000	O
O45	1.0	0.348014	0.322298	0.747650	Biso	1.000000	O
O46	1.0	0.838480	0.828943	0.755352	Biso	1.000000	O
O47	1.0	0.155099	0.176619	0.235526	Biso	1.000000	O
O48	1.0	0.656032	0.673641	0.243848	Biso	1.000000	O

Supplementary References

[S1] S. Yazdani, T. D. Huan, Y. Liu, R. Kashfi-Sadabad, R. D. Montaño, J. He, and M. T. Pettes, "Highly charged interface trap states in PbS_{1-x} govern electro-thermal transport," APL Mater. **7**, 071105 (2019). https://doi.org/10.1063/1.5096786

[S2] B. H. Toby and R. B. Von Dreele, "GSAS-II: The genesis of a modern open-source all purpose crystallography software package," J. Appl. Cryst. **46**, 544 (2013). https://doi.org/10.1107/S0021889813003531

[S3] A. L. Pope, B. Zawilski, and T. M. Tritt, "Description of removable sample mount apparatus for rapid thermal conductivity measurements," Cryogenics **41**, 725 (2001). https://doi.org/10.1016/S0011-2275(01)00140-0